Results of the Department of Space Physics, Institute of Atmospheric Physics, Czech Academy of Sciences, published in 2019

1. Multi-instrument observation of nonlinear EMIC-driven electron precipitation at sub-MeV energies

In recent years, experimental results have consistently shown evidence of electromagnetic ion cyclotron (EMIC) wave-driven electron precipitation down to energies as low as hundreds of keV. However, this is at odds with the limits expected from quasi-linear theory. Recent analysis using nonlinear theory has suggested energy limits as low as hundreds of keV, consistent with the experimental results, although to date this has not been experimentally verified. In this study, we have presented concurrent observations from Polar-orbiting Operational Environmental Satellite, Radiation Belt Storm Probes, Global Positioning System, and ground-based instruments, showing concurrent EMIC waves and sub–MeV electron precipitation, and a global dropout in electron flux. We have shown through test particle simulation that the observed waves are capable of scattering electrons as low as hundreds of keV into the loss cone through nonlinear trapping, consistent with the experimentally observed electron precipitation.

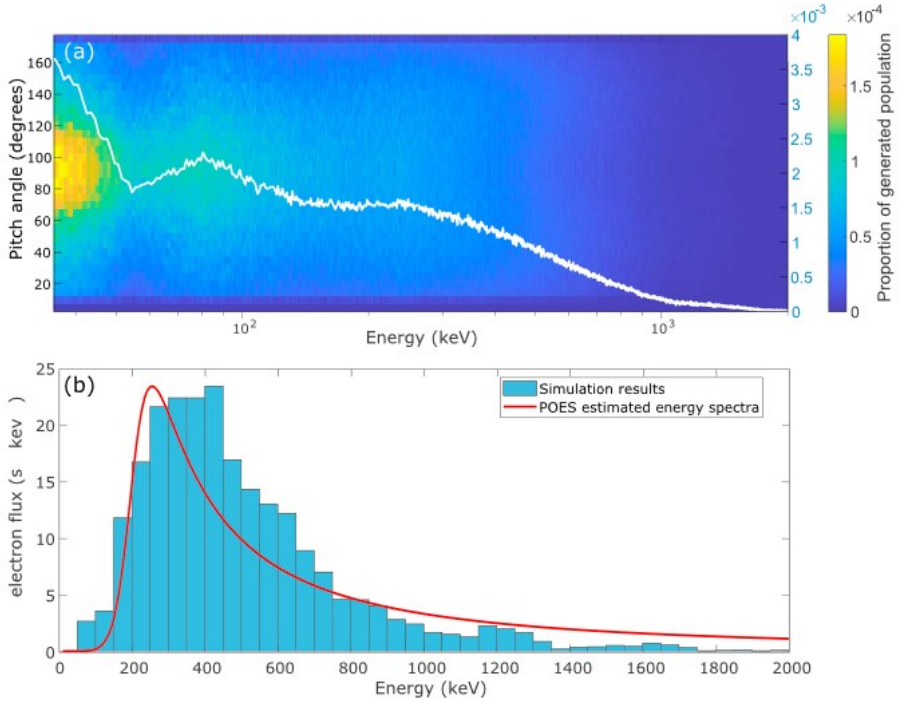

Distribution of the generated electrons in energy and pitch angle. The white line represents the energy spectrum of this distribution summed across all pitch angles. The scales on the right represent the proportion of the total generated electron population. (b) Comparison of the POES-derived electron precipitation flux spectrum (red line) with the precipitation predicted by the test particle simulation between 119 and 120 s (cyan histogram)

Reference:

Hendry, A. T., Santolík, O., Kletzing, C. A., Rodger, C. J., Shiokawa, K., & Baishev, D. (2019). Multi-instrument observation of nonlinear EMIC-driven electron precipitation at sub-MeV energies. Geophysical Research Letters,46, 7248-7257. https://doi.org/10.1029/2019GL082401.

Related references:

Hendry, **Aaron T.,** Mark A. Clilverd, Craig J. Rodger, Mark J. Engebretson (2019) , Chapter 8 - Ground-based very-low-frequency radio wave observations of energetic particle precipitation, The Dynamic Loss of Earth's Radiation Belts, From Loss in the Magnetosphere to Particle Precipitation in the Atmosphere, Book , edited by Allison N. Jaynes and Maria E. Usanova

Miyoshi, Y., Matsuda, S., Kurita, S.,Nomura, K., Keika, K., Shoji, M., N. Kitamura, Y. Kasahara, A. Matsuoka, I. Shinohara, K. Shiokawa, S. Machida, **O. Santolik**, S. A. Boardsen, R. B. Horne, and J. F. Wygant (2019). EMIC waves converted from equatorial noise due to M/Q= 2 ions in the plasmasphere: Observations from Van Allen Probes and Arase. Geophysical Research Letters,46,5662-5669. https://doi.org/10.1029/2019GL083024

Rodger, C. J., Turner, D. L., Clilverd, M. A., & **Hendry, A. T.** (2019). Magnetic local time-resolved examination of radiation belt dynamics during high-speed solar wind speed-triggered substorm clusters. Geophysical Research Letters, 46, 10,219–10,229. https://doi.org/10.1029/2019GL083712.

Lessard, M. R., Paulson, K., Spence, H. E., Weaver, C., Engebretson, M. J., Millan, R., et al. + **A. Hendry** (2019). Generation of EMIC waves and effects on particle precipitation during a solar wind pressure intensification with Bz > 0. Journal of Geophysical Research: Space Physics, 124, 4492–4508. https://doi.org/10. 1029/2019JA026477.

2. Effects of ducting on whistler mode chorus or exohiss in the outer radiation belt.

Previously published statistics based on Cluster spacecraft measurements surprisingly showed that in the outer radiation belt, lower band whistler mode waves predominantly propagate unattenuated parallel to the magnetic field lines up to midlatitudes, where ray tracing simulations indicated highly attenuated waves with oblique wave vectors. We have explained this behavior by considering a large fraction of ducted waves. We argue that these ducts can be weak and thin enough to be difficult to detect by spacecraft instrumentation while being strong enough to guide whistler mode waves in a cold plasma ray tracing simulation. After adding a tenuous hot electron population, we have obtained a strong effect of Landau damping on unducted waves, while the ducted waves experience less damping or even growth. Consequently, the weighted average of amplitudes and wave normal angles of a mixture of ducted and unducted waves has provided us with strong quasi-parallel waves, consistent with the observations.

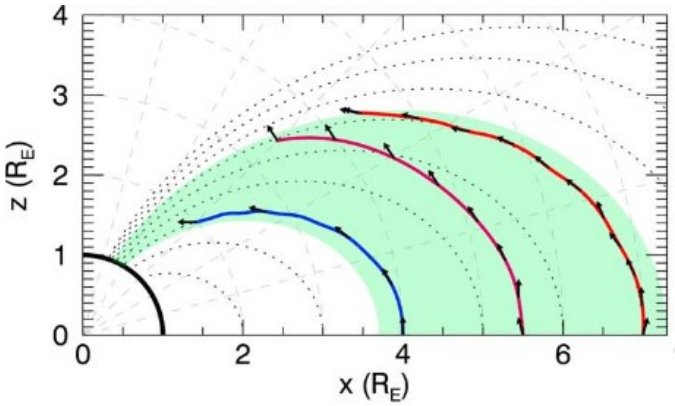

Ray trajectories in the meridional plane. Ducts are placed at L={4.0,5.5,7.0}and correspond to the initial distance of the blue, purple, and red rays, respectively. The width of the ducts is 96 km, and the relative density increase is 0.06. Black arrows represent the directions of wave vectors and are plotted with equidistant group time intervals of 0.1 s and at the end of the trajectory. Initial wave normal angles are 0◦for the blue trajectory, −15◦for the purple trajectory, and 15◦for the red trajectory.

Reference:

Hanzelka, M., & Santolik, O. (2019). Effects of ducting on whistler mode chorus or exohiss in the outer radiation belt. Geophysical Research Letters, 46, 5735-5745. https://doi.org/10.1029/2019GL083115.

Related references:

Hartley, D. P., Kletzing, C. A., Chen, L., Horne, R. B., & **Santolík, O.** (2019). Van Allen Probes observations of chorus wave vector orientations: Implications for the chorus-to-hiss mechanism. Geophysical Research Letters, 46, 2337-2346. https://doi.org/10.1029/2019GL082111,

Ripoll, J.-F., Loridan, V., Denton, M. H., Cunningham, G., Reeves, G., **Santolík, O.**,et al. (2019). Observations and Fokker-Planck simulations of the L-shell, energy, and pitch angle structure of Earth's electron radiation belts during quiet times. Journal of Geophysical Research: Space Physics,124, 1125–1142. https://doi.org/10.1029/2018JA026111

3. Direct measurement of low-energy electron foreshock beams

Electrostatic plasma waves above and below the local electron plasma frequency represent a characteristic feature of the foreshock region. These waves are known to be generated by electron beams originating from the bow shock and their spectrum varies from narrowband intense waves close to foreshock edge to weaker broadband emissions further downstream. We have presented a statistical analysis of electron beams observed in the terrestrial foreshock by the Cluster spacecraft. We compared the energy of foreshock electron beams with the spectrum of electrostatic waves and established a clear correspondence between beam energy and spectrum of the waves. The broadband emissions are correlated with low-energy beams, while high-energy electron beams are associated with narrowband Langmuir waves. Next we solved the linear dispersion relation for a subset of observed electron plasma

distributions. We discovered that while the observed electron distributions often exhibit a “bump on tail” feature necessary for an instability, the observed combination of beam energy, density, and temperature typically corresponds to a stable situation. This indicates that strongly unstable electron beams are quickly dissipated by the quasi-linear processes and only stable or marginally stable beams persist long enough to be observed by the instrument.

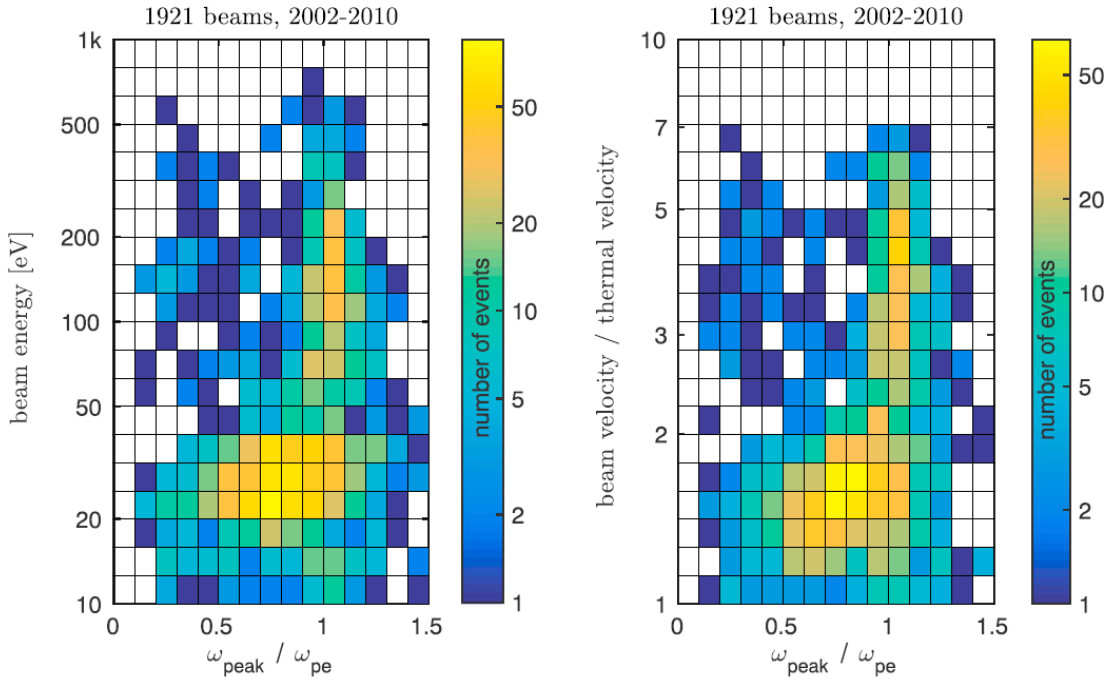

Distribution of beam energy versus relative frequency of the largest peak in the electric field spectrum constructed from the statistical data set of C2 measurements from 2002 to 2010. (left) Joint two-dimensional histogram of beam energy in electron volts versus the relative frequency. (right) Analogous histogram with beam velocity normalized to the thermal velocity on the vertical axis. Color coded is the number of identified beams whose energy falls in the corresponding energy bin and frequency in the frequency bin simultaneously.

Reference:

Soucek, J., Pisa, D., & Santolik, O. (2019). Direct measurement of low-energy electron foreshock beams. Journal of Geophysical Research: Space Physics, 124, 2380-2392 https://doi.org/10.1029/2019JA026470

Related references:

Ala-Lahti, M., Kilpua, E. K. J., **Souček, Jan**, Pulkkinen, T. I., Dimmock, A. (2019), Alfvén Ion Cyclotron Waves in Sheath Regions Driven by Interplanetary Coronal Mass Ejections, Journal of Geophysical Research: Space Physics, 124, 6, pp. 3893-3909

4. Evidence for low density holes in Jupiter's ionosphere

Intense electromagnetic impulses induced by Jupiter's lightning have been recognized to produce both low-frequency dispersed whistler emissions and non-dispersed radio pulses. We have collaborated on a discovery of electromagnetic pulses associated with Jovian lightning. Detected by the Juno Waves instrument during its polar perijove passes, the dispersed millisecond pulses called Jupiter dispersed pulses (JDPs) provide evidence of low density holes in Jupiter's ionosphere. 445 of these JDP emissions have been observed in snapshots of electric field waveforms. Assuming that the maximum delay occurs in the vicinity of the free space ordinary mode cutoff frequency, we have estimated the characteristic plasma densities and lengths of plasma irregularities along the line of propagation from lightning to Juno. These irregularities show a direct link to low plasma density holes with less than 250 particles in one cubic centimeter in the nightside ionosphere.

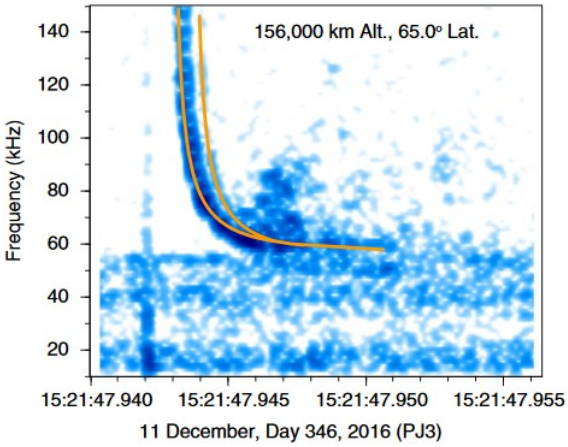

Example of Jupiter dispersed pulses (JDPs). The spectrogram was converted from a 16.384-ms waveform snapshot. The orange curves are fitted via the O mode propagation model to a pair of JDPs with a pulse-to-pulse interval of 0.7 ms.

Reference:

Imai, M**., Kolmasová, I.**, Kurth, W.S., **Santolík, O.**, Hospodarsky, G. B., Gurnett, D.A., Brown, S. T., Bolton, S.J., Connerney, J. E. P., Levin, S. M. Evidence for low density holes in Jupiter's ionosphere. Nature Communications 10, 2751 (2019) doi:10.1038/s41467-019-10708-w

Related references:

Menietti, J. D., Yoon, P. H**., Pisa, D.**, Averkamp, T. F., Sulaiman, A. H.,Kurth, W. S., **Santolík, O.,** Arridge, C. S. (2019). The role of intense upper hybrid resonance emissions in the generation of Saturn narrowband emission. Journal of Geophysical Research: Space Physics, 124, 5709-5718. https://doi.org/10.1029/2019JA026855.

Menietti, J. D., B. Palmaerts**, J. Zahlava**, T. F. Averkamp, J. B. Groene, and W. S. Kurth (2019), Quasi-periodic Saturn auroral hiss observed during a Cassini proximal orbit, Geophysical Research Letters, doi: 10.1029/2019JA027338

Sulaiman, A. H., Farrell, W.M., Ye, S. - Y., Kurth, W. S., Gurnett, D. A., Hospodarsky, G. B., Menietti, J. D., **Píša, David**, Hunt, G.J., Agiwal, O., Dougherty, M. K. , 2019: A persistent, large-scale, and ordered electrodynamic connection between Saturn and its main rings, Geophysical Research Letters, 46, 13, pp. 7166-7172

Ye, S. - Y., Vaverka, (...), **Píša, D.,** Hospodarsky, G. B., Kurth, W. S., Horanyi, M., 2019: Understanding Cassini RPWS Antenna Signals Triggered by Dust Impacts, Geophysical Research Letters, 46, 20, pp. 10941-10950

5. Lightning contribution to overall whistler mode wave intensities in the plasmasphere

We have analyzed contribution of thunderstorms to the intensity of electromagnetic radiation at audible frequencies observed at altitudes between 600 and 32,000 km, where these waves can influence the Van Allen radiation belts. We have used the World Wide Lightning Location Network to obtain information about lightning locations and times. Based on that, a lightning activity level has been assigned to individual electromagnetic wave measurements of two spacecraft missions: DEMETER and Van Allen Probes. Subsequently, we compare median wave intensities obtained at the times of high and low lightning activity. Their ratio reveals that the radio waves originating in strong lightning storms can significantly overpower all other natural waves in a wide range of frequencies and L-shells. The strength of this effect substantially depends on the local time. Specifically, it is the best pronounced in the afternoon/evening/night sector and nearly absent in the morning/noon sector. This agrees with the local time dependence of both, lightning occurrence and the wave attenuation in the ionosphere. The observed lightning contribution mainly occurs at frequencies over 500 Hz and with a bandwidth decreasing from 12 to 4 kHz for L between 1.5 and 5.

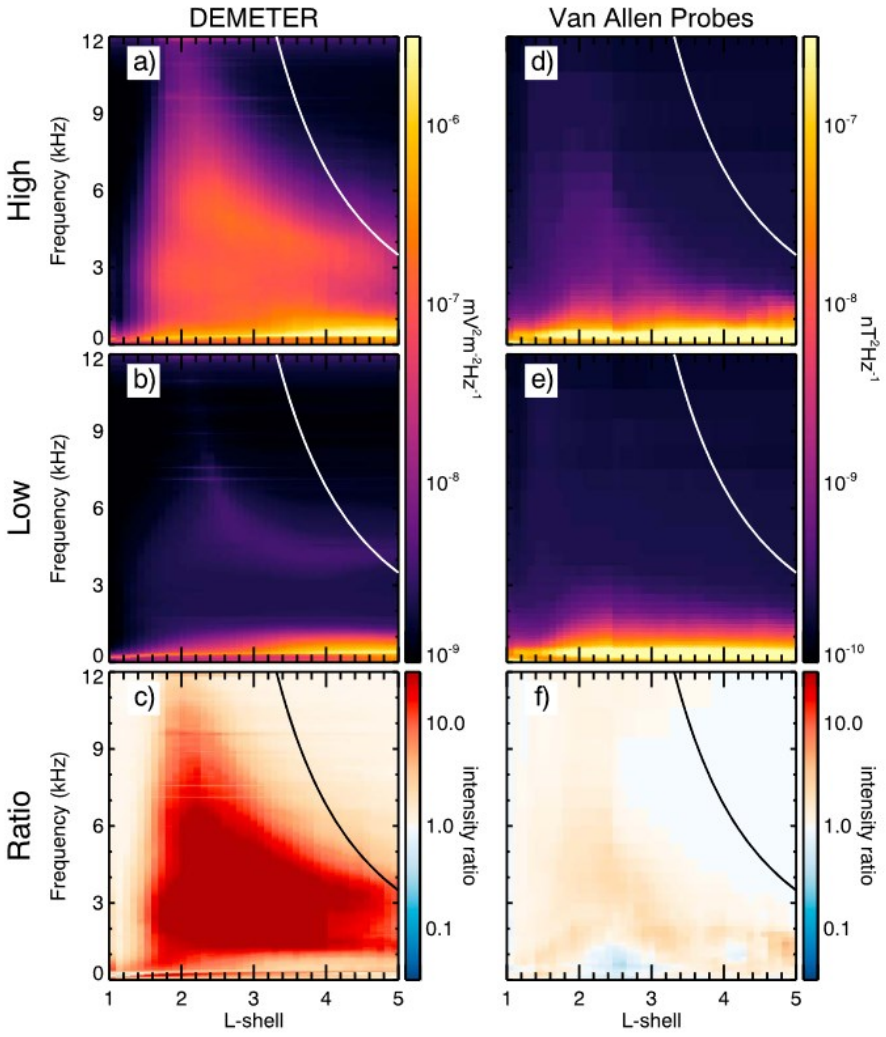

(a, b) Color-coded median power spectral density of electric field fluctuations measured by the DEMETER spacecraft during the morning side half-orbits at the times of high and low lightning activity, respectively. (c) Ratio between the panels (a) and (b). The red color in panel (c) corresponds to the median wave intensity being larger at the times of high lightning activity than that at the times of low lightning activity. The white color corresponds to the lightning contribution being negligible, and the blue color corresponds to the median wave intensity at the times of low lightning activity being larger than that at the times of high lightning activity. The solid black or white curves mark half of the equatorial electron gyrofrequency calculated using a dipole magnetic field model. (d–f) Same as (a)–(c) but for magnetic field measurements performed by the Van Allen Probes inside the plasmasphere in the MLT interval from 9 to 12 hr.

Reference:

Záhlava, J., Nemec, F**., Santolík, O., Kolmasová, I.**, Hospodarsky, G. B., Parrot, M., et al. (2019). Lightning contribution to overall whistler mode wave intensities in the plasmasphere. Geophysical Research Letters, 46, 8607-8616. https://doi.org/10.1029/2019GL083918.

Related references:

Macotela, E. L., Němec, F., Manninen, J., **Santolík, O., Kolmašová, I.,** & Turunen, T. (2019). VLF emissions with banded structure in the 16- to 39-kHz frequency range measured by a high-latitude ground-based receiver. Geophysical Research Letters, 46. https://doi.org/10.1029/2019GL086127.

Pasmanik, D. L., Demekhov, A. G.,**Hayosh, M.**, Nemec, F., **Santolík, O**.,& Parrot, M. (2019). Quasiperiodic ELF/VLF emissions detected onboard the DEMETER spacecraft: Theoretical analysis and comparison with observations. Journal of Geophysical Research: Space Physics, 124, 5278-5288. https://doi.org/10.1029/2018JA026444.

Xia, Z., Chen, L., Zhima, Z**., Santolik, O**., Horne, R. B., & Parrot, M. (2019). Statistical characteristics of ionospheric hiss waves. Geophysical Research Letters, 46, 7147-7156. https://doi.org/10.1029/2019GL083275,

Bezdeková, B., Nemec, F., Parrot, M., **Hajos, M., Záhlava, J., & Santolík, O.** (2019). Dependence of properties of magnetospheric line radiation and quasiperiodic emissions on solar wind parameters and geomagnetic activity. Journal of Geophysical Research: Space Physics, 124, 2552- 2568. https://doi.org/10.1029/2018JA026378,

6. Initial breakdown pulses accompanied by VHF pulses during negative cloud-to-ground lightning flashes

There is a lack of understanding of how a lightning flash initiates, as this process usually takes place deep inside thunderclouds. Electromagnetic pulses emitted during lightning initiation, which can be measured from a safe distance, help us to understand lightning better. We have used arrays of low-frequency (~0–2.5 MHz) and very high frequency (186–192 MHz) receivers and compared their recordings registered during initiation of 20 cloud-to-ground lightning flashes. We have found that the larger pulses detected during lightning initiation in low-frequency records were systematically accompanied by pulses detected in the very high frequency records. This observation indicates that the initial lightning extension process occurs very fast and at multiple length scales and that emitted electromagnetic radiation covers a very large range of frequencies.

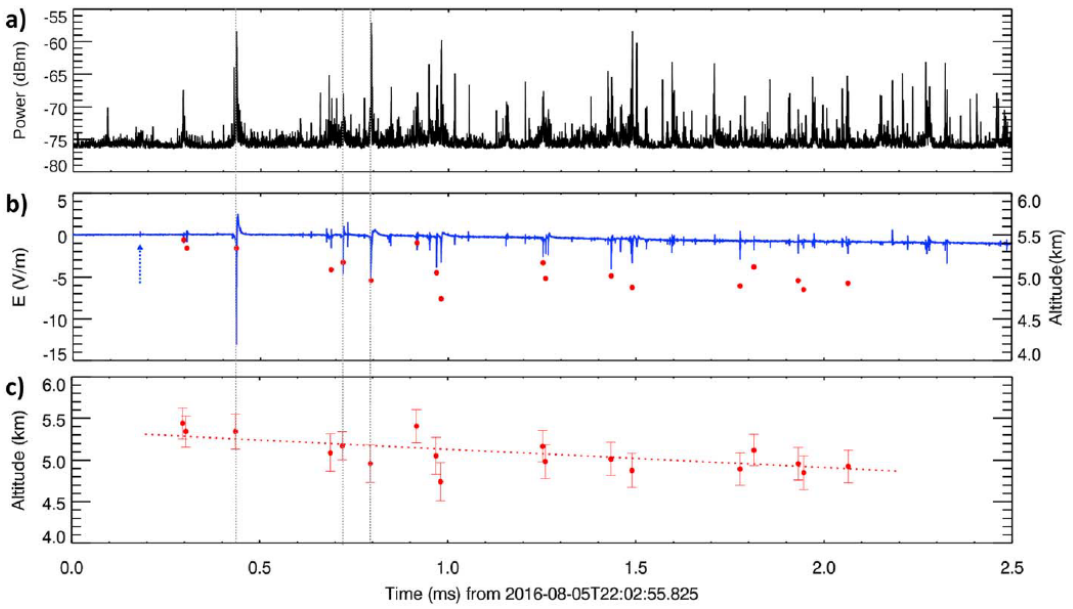

Examples of Fast Antenna and LogRF data recorded at the EE station on 5 August 2016. The black curve represents the calibrated waveform measured by the LogRF receiver, and the blue curve represents the calibrated waveforms recorded by the broadband E-change receiver. A blue arrow indicates the time of occurrence of the first recognizable pulse in Fast Antenna records used as a start of the investigated 2-ms-long waveform capture. Red dots plotted in panels (b) and (c) point at the occurrence heights of individual initial breakdown pulses calculated using the Position By Fast Antenna method. Vertical grey dotted lines identify very high frequency pulses occurring within durations of classical initial breakdown pulses. Dotted red line in panel (c) represents a linear trend indicating the downward propagation of developing discharge.

Reference:

Kolmašová, I., Marshall, T., Bandara, S., Karunarathne, S., Stolzenburg, M., Karunarathne, N., & Siedlecki, R. (2019). Initial breakdown pulses accompanied by VHF pulses during negative cloud-to-ground lightning flashes. Geophysical Research Letters, 46, doi:10.1029/2019GL082488.

Related references:

Marshall, T., Bandara, S., Karunarathne, N., Karunarathne, S., **Kolmašová, Ivana**, Siedlecki, R., Stolzenburg, M. (2019): A study of lightning flash initiation prior to the first initial breakdown pulse, Atmospheric Research, 217, 1, pp. 10-23

J. Slegl, **J. Minárová**, P. Kuca**, I. Kolmasová, O. Santolík, Z. Sokol**, G. Reitz, I. Ambrozová and O. Ploc (2019), response of the Czech RMN network to thunderstorm activity, Radiation Protection Dosimetry, pp. 1–4, doi:10.1093/rpd/ncz205

Enrico Arnone, József Bór, Olivier Chanrion, Veronika Barta, Stefano Dietrich, Carl-Fredrik Enell, Thomas Farges, Martin Füllekrug, Antti Kero, Roberto Labanti, Antti Mäkelä, Keren Mezuman, Anna Odzimek, **Martin Popek**, Marco Prevedelli, Marco Ridolfi, Serge Soula, Oscar van der Velde, Yoav Yair, Przemyslaw

Zoladek, and Torsten Neubert (2019), Climatology of transient luminous events and lightning observed above Europe and the Mediterranean Sea, Surv Geophys, doi:10.1007/s10712-019-09573-5

7. Statistical Survey of Coronal Mass Ejections and Interplanetary Type II Bursts

Coronal mass ejections(CMEs)are responsible for most severe space weather events, such as solar energetic particle events and geomagnetic storms at Earth. Type II radio bursts are slow drifting emissions produced by beams of suprathermal electrons accelerated at CME-driven shock waves propagating through the corona and interplanetary medium. We have reported a statistical study of 153 interplanetary type II radio bursts observed by the two STEREO spacecraft between 2008 March and 2014 August. The shock associated radio emission was compared with CME parameters included in the Heliospheric Cataloguing, Analysis and Techniques Service catalog. We found that faster CMEs are statistically more likely to be associated with the interplanetary type II radio bursts. We have correlated frequency drifts of interplanetary type II bursts with white-light observations to localize radio sources with respect to CMEs. Our results suggest that interplanetary type II bursts are more likely to have asource region situated closer to CME flanks than CME leading edge regions.

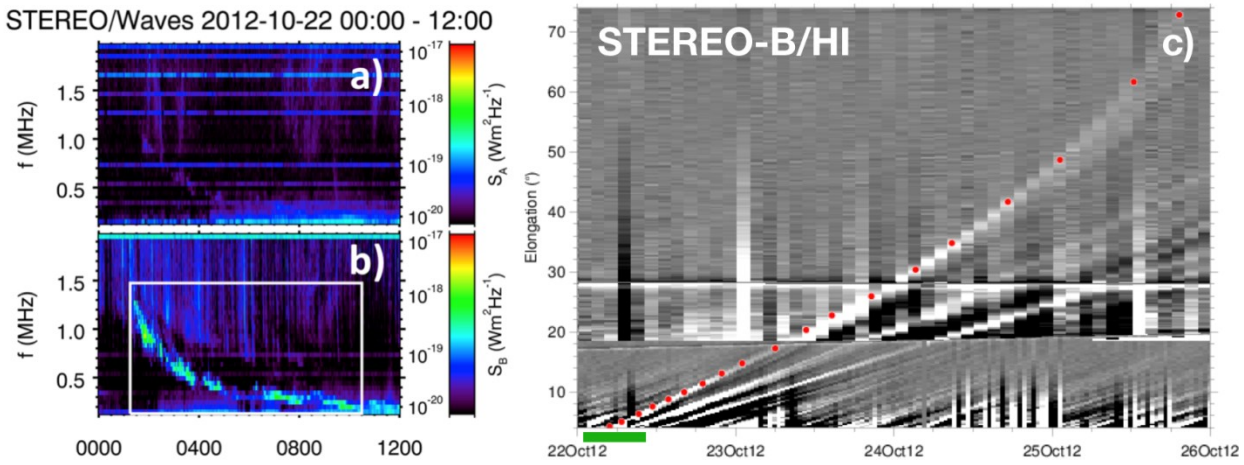

Radio and white-light measurements by STEREO. (a), (b) Radio flux density S between 2012 October 22 00:00 UT and 12:00 UT at STEREO-A and STEREO-B, respectively. A white rectangle denotes the type II burst. (c) STEREO-B/HI time-elongation map between 2012 October 22 and 26. Positions of the CME are denoted as red circles. A green bar shows a time interval with the radio emission.

Reference:

V. Krupar , J. Magdalenić , J. P. Eastwood , N. Gopalswamy , **O. Kruparova** , A. Szabo , and F. Němec (2019), Statistical Survey of Coronal Mass Ejections and Interplanetary Type II Bursts, The Astrophysical Journal, 882:92 (5pp), https://doi.org/10.3847/1538-4357/ab3345.

Related reference:

Kontar, Eduard P.; Chen, Xingyao; Chrysaphi, Nicolina; Jeffrey, Natasha L. S.; Emslie, A.Gordon; **Krupar, Vratislav;** Maksimovic, Milan; Gordovskyy, Mykola; Browning, Philippa K. (2019), Anisotropic Radio-wave Scattering and the Interpretation of Solar Radio Emission Observations, The Astrophysical Journal, 884, 2, article id. 122, 15 pp., https://iopscience.iop.org/article/10.3847/1538-4357/ab40bb

8. Statistical survey of the terrestrial bow shock observed by the Cluster spacecraft

The Sun is continuously emitting a stream of charged particles—called the solar wind—from its upper atmosphere. The terrestrial magnetosphere forms the obstacle to its flow. Due to supersonic speed of the solar wind, the bow shock is created ahead of the magnetosphere. This abrupt transition region between supersonic and subsonic flows has been frequently observed by the four Cluster spacecraft. Using a timing analysis, we have retrieved speed and directions of the bow shock motion for a large number of crossings. We have correlated the bow shock speed with the solar wind speed and predictions of the bow shock locations by the empirical model. A better understanding of the bow shock kinematics may bring new insights to wave-particle interactions with applications in laboratory plasmas.

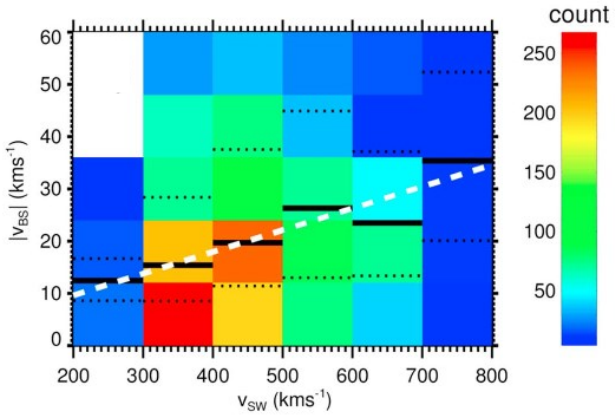

Statistical study of the bow shock speed. 2-D histogram of the number of events as a function of bow shock speed and the solar wind speed. Solid and dotted lines denote median values and the 25th/75th percentiles, respectively. A white dashed line shows a linear fit.

Reference:

Kruparova, O., Krupar, V.,Safrankova, J., Nemecek, Z.,Maksimovic, M., **Santolik, O.**, et al.(2019). Statistical survey of the terrestrial bow shock observed by the Cluster spacecraft. Journal of Geophysical Research: Space Physics,124, 1539-1547. https://doi.org/10.1029/2018JA026272

Department of Space Physics, Institute of Atmospheric Physics of the Czech Academy of Sciences in 2019

1. Radka Balková, secretary, 50% FTE
2. Zdeněk Griebl, technician, 40% FTE
3. Benjamin Grison, research scientist
4. Michajlo Hajoš, research scientist
5. Miroslav Hanzelka, PhD student, 70% FTE
6. Aaron T. Hendry, postdoctoral associate
7. Petr Kašpar, postdoctoral associate
8. Ivana Kolmašová, research scientist
9. Andrea Kolínská, MSc student, 50% FTE
10. Vratislav Krupař, research scientist, 50%FTE
11. Oksana Krupařová, research scientist, 48% FTE
12. Radek Lán, research engineer
13. Jan Lukačevič, PhD student, 70% FTE
14. David Píša, research scientist
15. Martin Popek, TLE observer, 25% FTE
16. Ondřej Santolík, senior research scientist, head of the department
17. Jan Snížek, research engineer, since June 1, 50% FTE
18. Jan Souček, senior research scientist, deputy head of the department
19. Hana Špačková, PhD student, 70% FTE
20. Ulrich Taubenschuss, research scientist
21. *Alexander Tomori, PhD student, parental leave*
22. Luděk Uhlíř, research engineer
23. Christof Weber, postdoctoral associate
24. Jan Záhlava, PhD student, since April 1, 20% FTE